Smart Structures and Systems, *Vol. 24, No. 1 (2019) 127-139*
DOI: https://doi.org/10.12989/sss.2019.24.1.127

Seismic damage mitigation of bridges with self-adaptive SMA-cable-based bearings

Yue Zheng[1,2], You Dong[3], Bo Chen[*4] and Ghazanfar Ali Anwar[3]

[1]*Department of Bridge Engineering, Tongji University, Shanghai, China*
[2]*Department of Civil and Environmental Engineering, University of California, Berkeley, USA*
[3]*Department of Civil and Environmental Engineering, The Hong Kong Polytechnic University, Hong Kong, China*
[4]*Key Laboratory of Roadway Bridge and Structural Engineering, Wuhan University of Technology, Wuhan, China*

(Received August 11, 2018, Revised February 22, 2019, Accepted February 27, 2019)

Abstract. Residual drifts after an earthquake can incur huge repair costs and might need to replace the infrastructure because of its non-reparability. Proper functioning of bridges is also essential in the aftermath of an earthquake. In order to mitigate pounding and unseating damage of bridges subjected to earthquakes, a self-adaptive Ni-Ti shape memory alloy (SMA)-cable-based frictional sliding bearing (SMAFSB) is proposed considering self-adaptive centering, high energy dissipation, better fatigue, and corrosion resistance from SMA-cable component. The developed novel bearing is associated with the properties of modularity, replaceability, and earthquake isolation capacity, which could reduce the repair time and increase the resilience of highway bridges. To evaluate the super-elasticity of the SMA-cable, pseudo-static tests and numerical simulation on the SMA-cable specimens with a diameter of 7 mm are conducted and one dimensional (1D) constitutive hysteretic model of the SMAFSB is developed considering the effects of gap, self-centering, and high energy dissipation. Two types of the SMAFSB (i.e., movable and fixed SMAFSBs) are applied to a two-span continuous reinforced concrete (RC) bridge. The seismic vulnerabilities of the RC bridge, utilizing movable SMAFSB with the constant gap size of 60 mm and the fixed SMAFSBs with different gap sizes (e.g., 0, 30, and 60 mm), are assessed at component and system levels, respectively. It can be observed that the fixed SMAFSB with a gap of 30 mm gained the most retrofitting effect among the three cases.

Keywords: self-adaptively resilient bridges; SMA-cable-based bearing; seismic vulnerability analysis; probabilistic seismic damage method

1. Introduction

Bridges being one of the essential infrastructure components are prone to damage under seismic hazards. In recent years, seismic isolation has become a common approach to reduce bridge damage located in earthquake-prone regions. Various types of seismic isolation devices are used in the literature for seismic damage mitigation of bridges such as lead-rubber bearings, high damping bearings, friction pendulum bearing, steel plate dampers and magneto-rheological dampers (Ghobarah and Ali 1990, Warn and Whittaker 2004, Bhuiyan *et al*. 2009). These isolation devices reduce the amount of seismic energy transferred to the bridge structure by introducing discontinuity between the components of a structure. Traditional isolation devices have been used for seismic hazard mitigation, but they have certain disadvantages in terms of durability, aging, maintenance, long-term reliability and residual drifts (Dolce *et al*. 2000, Dion *et al*. 2011, 2012, Dong *et al*. 2016, a, b; Su *et al*. 2019). In order to overcome this problem, shape memory alloy (SMA) is recently gaining much popularity, characterized by its high strength, super-elasticity, energy dissipation, better fatigue and corrosion resistance (Song *et al*. 2006, Ozbulut *et al*. 2011, Fang *et al.* 2014, 2017, Qiu and Zhu 2017a, b, Qiu *et al*. 2017, 2018, Fang *et al*. 2019). SMA applications in civil infrastructure can be classified into demand reducing systems and energy dissipation systems as shown in Fig. 1. Demand reducing systems include SMA bars, SMA wire re-centering devices, SMA spring isolation devices, SMA tendon isolation devices, while energy dissipation systems include SMA bracings, SMA dampers and connection elements. Different studies utilize SMA as a demand reducing or energy dissipating component for the improved seismic performance of bridge infrastructure

Choi *et al.* (2005, 2006), for example, proposed an isolation elastomeric bearing with SMA wires to recover the residual displacement between adjacent decks of bridges. Dezfuli and Alam (2014, 2016) later improved and proposed two types of SMA-wire-based elastomeric bearings having superior self-centering property and better energy dissipation capacity as compared to conventional elastomeric bearings. However, the proposed isolation bearing with SMA wires had limit restoring force. Yuan *et al*. (2012) developed a frictional sliding bearing incorporating traditional tendons to reduce seismic demands on bridges, though the tendon-based bearing was found incapable of providing energy dissipation capacity and may cause damage to the RC pier. Zheng *et al*. (2018), Zheng and Dong (2018) used shape memory alloy in the

∗Corresponding author, Professor
E-mail: cbsteven@163.com

http://www.techno-press.com/journals/sss&subpage=7
ISSN: 1738-1584 (Print), 1738-1991 (Online)

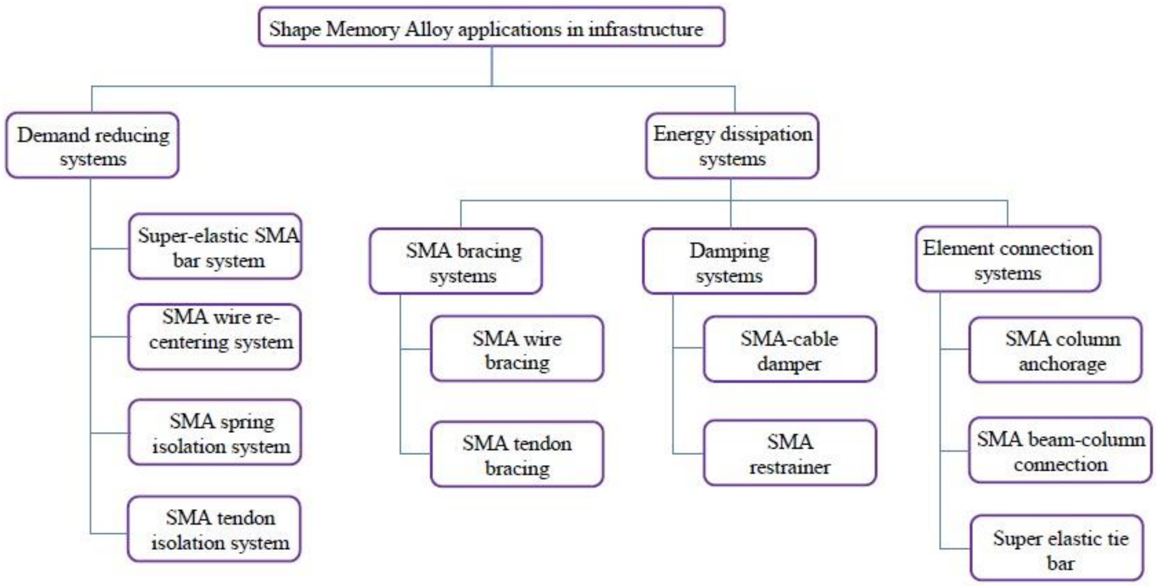

Fig. 1 Shape memory alloy applications in civil infrastructure

performance assessment and retrofit of civil infrastructure by considering long term benefits of SMA-cable-based friction sliding bearings on the proposed novel smart bridge emphasizing on the life-cycle performance bridge infrastructure. The effectiveness of SMA-cable based bearing in improving seismic performance in the long-term time interval was verified, however it was also concluded that the fixed SMA-cable-based bearing without gap can increase seismic demands on the bridge pier. Therefore, a new generation of the SMA-cable-based bearing is proposed, named SMAFSB. The SMAFSB with slack SMA-cable components reduce the earthquake-induced seismic demands on the bridge by increasing its fundamental time period. The SMAFSB also improves energy dissipation capacity resulting in further reduction of the seismic demands. The gap size not only affects the initial stiffness and shear capacity of the bearing, but also the seismic demands on vulnerable components such as RC pier and SMAFSB. The appropriate length of SMA-cable used in SMAFSB can be an effective self-adaptive seismic isolation strategy.

In this paper, the configuration of the modular SMAFSB is introduced. Series of tests are conducted on the SMA-cable specimens to investigate the behavior under pseudo-static loadings and one dimensional (1D) constitutive model for the self-adaptive SMAFSB is developed as a result. In addition to the sliding effect of the frictional sliding bearing, developed constitutive model also include the gap size, energy dissipation and self-centering effects of the SMA-cable component. To evaluate the feasibility and reliability of the proposed SMAFSB for seismic mitigation of bridges, a two-span continuous RC bridge constructed in the earthquake-prone region is considered as an example to conduct vulnerability analysis at both component and system levels.

2. Hysteretic model of SMAFSB

2.1 Design of SMAFSB

In addition to the inherit properties of self-centering, enhanced energy dissipation, better fatigue and corrosion resistance, the additional properties of modularity, replaceability and self-adaptability are also crucial considerations in the proposed SMAFSB. Like traditional bearing, the SMAFSB is also divided into three categories in terms of movement direction: unidirectionally movable SMAFSB, which is only allowed to move in the longitudinal or transversal direction of bridges; bidirectionally movable SMAFSB, can move in both the longitudinal and transversal directions, and the fixed SMAFSB, is restricted in both the longitudinal and transversal directions. For instance, as indicated in Fig. 2 the fixed SMAFSB is comprised of one fixed frictional sliding bearing component and two SMA-cable components. The main parts of the fixed frictional sliding bearing component include the top and bottom plates with screwed holes, a Teflon plate, a stainless-steel plate, an elastomeric pad, and a shear key. The SMA-cable component is made up of SMA cables and their anchorage parts. The fixed frictional sliding bearing component is capable of reducing seismic demands acting on RC piers or abutments because the shear force transmitted to the pier or abutment across the isolation interface can be controlled in a safe range by adjusting the coefficient of friction as low as possible after the shear key is broken under severe earthquakes. In other words, when the earthquake-induced shear force exceeds the shear capacity of the shear key, the interface between the sliders may slide resulting in reduced seismic demands on the bridge pier or abutments. Usually, the shear resistant capacity of the fixed sliding component only provides 10% of the bearing capacity which could not effectively prevent bridges from unseating during severe earthquakes.

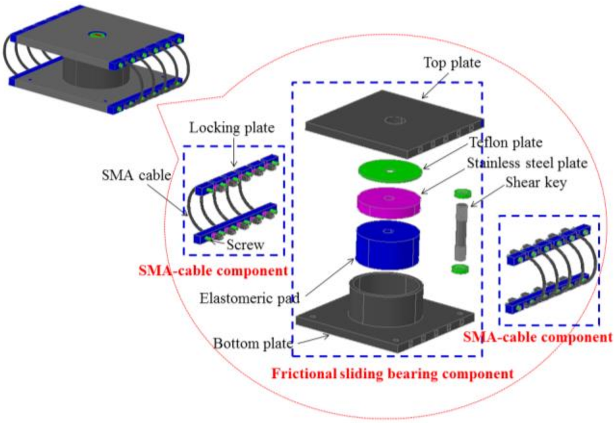

Fig. 2 Configuration of the fixed SMAFSB

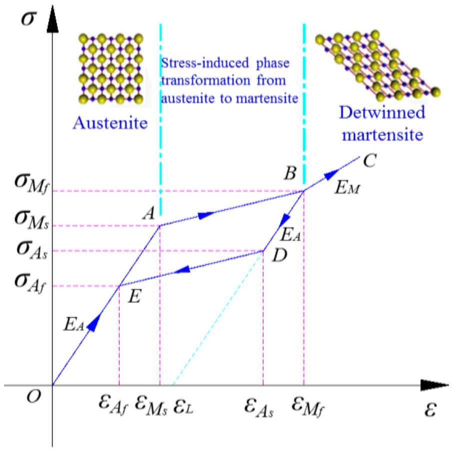

Fig. 3 Flag-shaped hysteretic model of the SMA cable

Therefore, two SMA-cable components are designed to be installed on the SMAFSB providing a restoring force up to 30% or more of the bearing capacity. Once the ultimate strength of the SMA cables is determined, the cross area of the SMA-cable component can be calculated and the gap size of the movable SMAFSB can be designed according to the service loads. However, the gap size of the fixed SMAFSB, as a variable and sensitive parameter, should be carefully investigated to ensure both the relative displacement of the bearing and external force acting on the vulnerable RC piers with fixed SMAFSB to be within acceptable limits during earthquakes. In conclusion, the resilient SMAFSB can not only retrofit seismic damage to bridges by increasing the natural period, but also prevent from unseating and pounding by keeping the displacement of the girder in an acceptable range during earthquakes. Furthermore, SMAFSB also exhibits self-adaptive centering and energy dissipation capacities.

2.2 Constitutive hysteretic model of SMA cables

As one family member of the SMA products, the SMA cable also has the mechanical properties of shape memory effect (SME) and the super-elasticity (SE). The two inherent properties of the SMA cable result from of phase shift between the austenite and the martensite. The austenite is stable at high temperature and low stress whereas the martensite is stale at low temperature and high stress. In the stress-free state, the mechanical properties of the SMA cable depend on the working temperature. Commonly, the four critical temperature points (i.e., M_f, M_s, A_f and A_s) denote martensite finish temperature, martensite start temperature, austenite finish temperature and austenite start temperature, respectively. When the working temperature of the SMA cable is provided, the mechanical properties of the SMA cable can be determined. A linear relation was formulated to describe the dependence of the critical stresses associated with the critical temperature points to cause phase shift with temperature (Brinson 1993). The flag-shaped hysteretic model of the Ni-Ti SMA cable is shown in Fig. 3. In Fig. 3, σ_{M_s} and ε_{M_s} denote the critical stress and strain of the SMA cable at M_s, respectively; C_M and C_A present the slopes of the phase shift boundary at the martensite and austenite phases in terms of stress and temperature, respectively; E_M and E_A are Young's moduli at the martensite and austenite phases, respectively; σ_{M_f} and ε_{M_f} are the critical stress and strain at M_f,

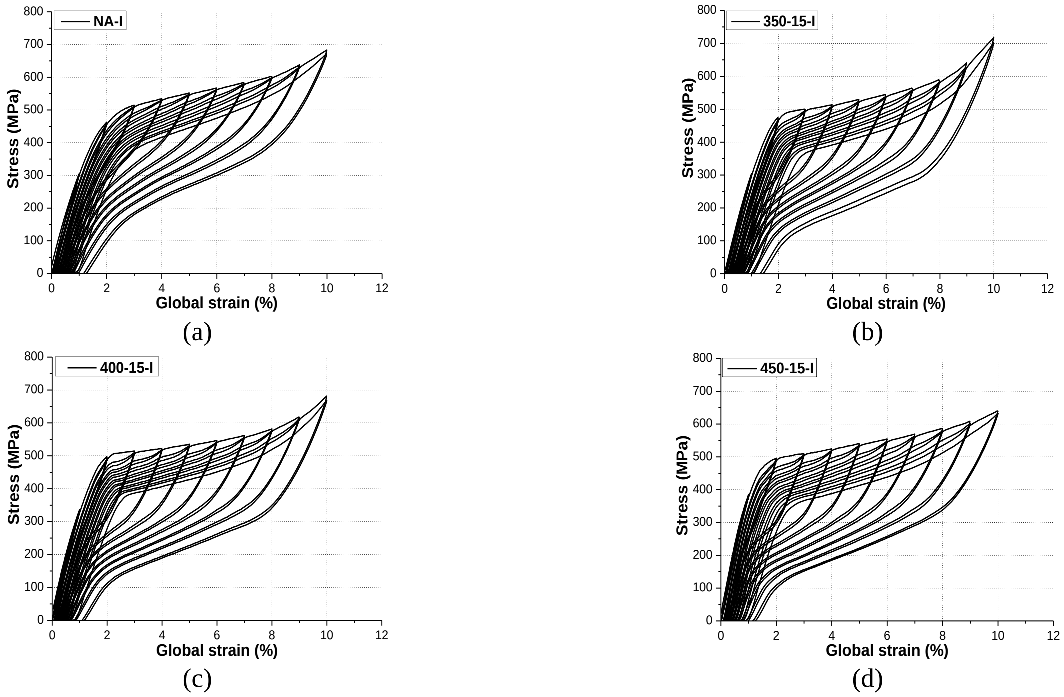

Fig. 4 Hysteretic behavior of SMA cables specimens

Table 1 Details of SMA cable specimens

Designation	Annealing temperature (℃)	Duration (mins)	Loading protocol	Maximum global strain
NA-I	N/A	N/A	Incremental	10%
350-15-I	350	15	Incremental	10%
400-15-I	400	15	Incremental	10%
450-15-I	450	15	Incremental	10%

respectively; σ_{A_s} and ε_{A_s} are the critical stress and strain at A_s, respectively; σ_{A_f} and ε_{A_f} are the critical stress and strain at A_f, respectively; T is the temperature at a reference state; and ε_L is the maximum residual strain. Liang and Rogers (1992) assumed that C_M is equal to C_A.

The SMA cable used in the proposed SMAFSB is made up of seven helically laid strands and each strand consists of seven helically wrapped monofilament wires with a diameter of 0.8 mm. This arrangement leads to a measured outer cable diameter of around 7 mm. The different SMA-cable specimens are cut from the same coil of cable, and the two ends of each specimen are firmly constrained to avoid unraveling. The specimens were then annealed via an electrical furnace at different targeting temperatures for varying durations, as summarized in Table 1. For ease of identification, each cable specimen was designated with a test code that starts with the annealing temperature and duration (NA indicates no annealing), followed by the incremental loading protocol. For instance, specimen 350-15-I10 means that the cable was subjected to a 350℃ annealing temperature for 15 minutes; the loading protocol is "increment cyclic loading" with a strain amplitude of 10%. The cable specimens are uniaxially loaded via a Universal Test Machine (UTM). Each end of the cable was fused and integrated into a hollow steel cylinder. Two ends were rigidly clamped by the top and bottom hydraulic wedge grips that match the external diameter of the cable. The load is recorded by a built-in load cell of the UTM, and the stress of the cable was calculated by dividing the load with the sum of the cross-sectional area of the 7 × 7 = 49 monofilament wires. The global strain-stress responses of all specimens under pseudo-static loads are shown in Fig. 4. All the cable specimens experienced anticipated axial elongations with no failure during the entire loading procedures. With increasing loading cycles, lateral "bending" was observed when the grip displacement returned to zero, but this slack deformation quickly vanished when the applied load was regained. This phenomenon is attributed to the accumulated residual strain which leads to a permanent cable elongation. In addition, certain degradations of the yield strength are observed in the SMA cables. Importantly, the SMA cables do exhibit

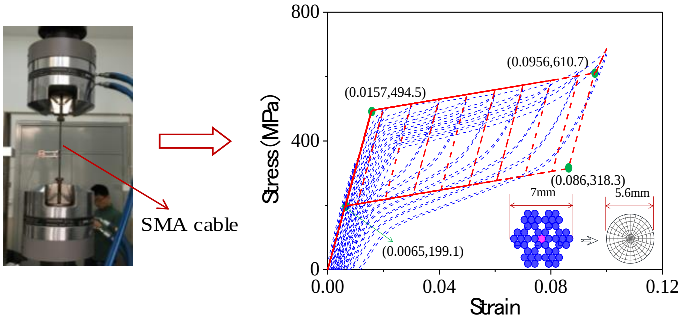

Fig. 5 Modelling of SMA-cable

Table 2 Key parameters of SMA-cable specimen

Strain	Magnitudes (%)	Stress	Magnitudes (MPa)
$\varepsilon_{\mathrm{Ms}}$	1.57	σ_{Ms}	494.5
$\varepsilon_{\mathrm{Mf}}$	9.56	σ_{Mf}	610.7
$\varepsilon_{\mathrm{As}}$	8.60	σ_{As}	318.3
$\varepsilon_{\mathrm{Af}}$	0.65	σ_{Af}	199.1

dependence on the annealing scheme. More recognizable flag-shaped behavior is shown for the specimens receiving an annealing temperature below 450℃. Compared with the non-annealed specimens, these annealed specimens seem to exhibit more distinguishable "yielding" strength and transformation plateaus, and in addition, slightly "wider" hysteretic loops. This may be related to the form setting property of the annealed cables. Apart from the possible deterioration of the SMA material itself, the significantly shifted transformation temperatures could also be a factor attributing to the less satisfactory hysteretic behavior. The SMA cables used in the proposed SMAFSB are assumed to be subjected to an annealing temperature of 400℃ for 15 minutes for its improvement in stiffness, energy dissipation, and form setting characteristics.

The flag-shaped model only requires a limited number of controlling parameters, which can be calibrated from the SMA-cable specimen results. To simulate the pseudo-static test results of the SMA cable specimen, a FE model is established using the open source program OpenSees (Mazzoni *et al*. 2007). A displacement-based fiber nonlinear element using a Self-centering material is employed to simulate the SMA cable. As demonstrated in Fig. 5, the cross-sectional area of all the 49 SMA wires in a SMA cable can be equivalent to an idealized circular section with a reduced diameter of 5.6 mm. The cross section of the element is divided into six layers along radius direction and each layer is divided into 24 fiber elements around circumference. Fig. 5 shows the numerical simulation result of a typical SMA cable (annealed at 400℃ for 15 minutes) together with the test result. The basic parameters for the model are given in Table 2. It is shown that the characteristic stresses and strains from the numerical simulation correlate well with the test results, although the degradation effect is not taken into account in the numerical model.

2.3 Constitutive hysteretic model of the SMAFSB

The SMAFSB is composed of a frictional sliding bearing and two SMA-cable components. Fig. 6(a) shows the configuration of the fixed SMAFSB. The lengths and widths of the top and bottom plates are denoted by A, C, and B, D, respectively, as shown in Fig. 6(b). The formula of the length (L) of each slack SMA-cable, shown in Fig. 6(c), can be computed as

$$L = \sqrt{H^2 + L_{xy}{}^2} \tag{1}$$

$$L_{xy} = \sqrt{(u_x + A - C)^2 + (u_y + B - D)^2} \tag{2}$$

in which H is the height between two anchorage points; L_{xy} is the projected length of the SMA-cable in the coordinate system (i.e., XOY); u_x and u_y represent the gaps of the SMA-cable component in the longitudinal and transversal directions, respectively.

The elastic-perfectly plastic force-displacement hysteretic model in Fig. 7(a) is used to model the seismic behavior of the frictional sliding bearing. The initial shear stiffness per unit length (k_e) and the sliding frictional force (F_s) of the frictional sliding bearing is expressed as

$$F_s = \mu N \tag{3}$$

in which μ is the frictional coefficient of the bearing component and N is the normal force bore by the frictional sliding bearing.

If the total cross-sectional area and the gaps in both the longitudinal and transversal directions of the SMA-cable component are known, the strain-stress hysteretic model of each SMA-cable can be converted into a 1D flag-shaped force-displacement hysteretic model of the SMAFSB in Fig.

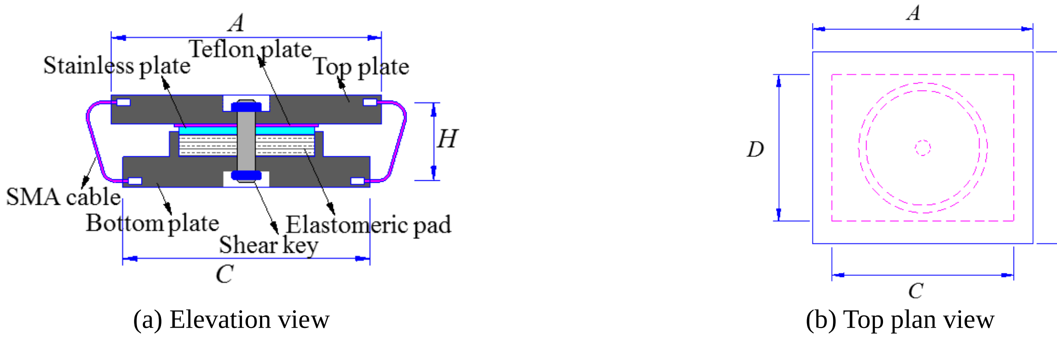

(a) Elevation view (b) Top plan view

(c) geometric relationships of the SMA-cable component

Fig. 6 Configuration and geometric dimensions of the SMAFSB

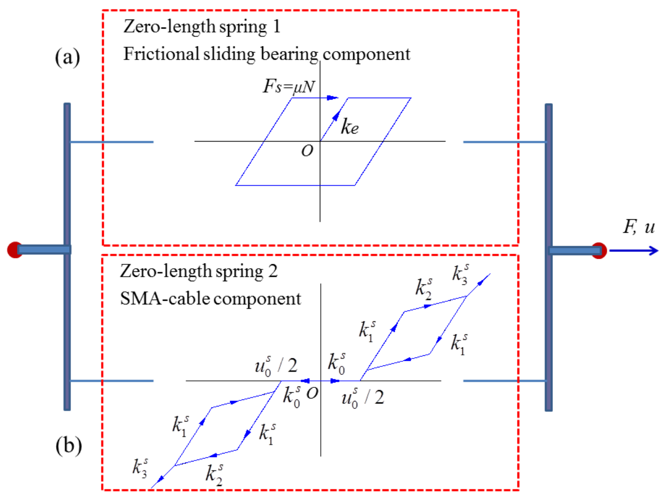

(a) Frictional sliding bearing component and (b) SMA-cable component

Fig. 7 Constitutive model of the SMAFSB

7(b). This model involves five parameters: u_0^s represents the gap of the SMA-cable component; k_0^s, k_1^s, k_2^s, and k_3^s present the axial tension stiffness per unit length of the slack SMA-cable, the initial axial tension stiffness per unit length, the yielding axial tension stiffness per unit length, and the super-elastic stiffness per unit length of the SMA-cable, respectively. The initial axial tension stiffness per unit length of the SMA-cable can be given as

$$k_1^s = \frac{E_A A_S}{L} \tag{4}$$

in which E_A is the initial Young's modulus of the SMA cables and A_s is the total cross-sectional area of all the SMA cables in the SMA-cable component. Herein, the frictional sliding bearing and the SMA-cable components are simulated by two zero-length spring elements in parallel.

3. Finite element modeling of the bridge

To assess the damage retrofitting efficiency of bridges equipped with the SMAFSBs subjected to earthquake events, seismic vulnerability analysis is conducted on a two-span reinforced concrete (RC) continuous girder bridge (20 + 20 m). The topological layout of the bridge is shown

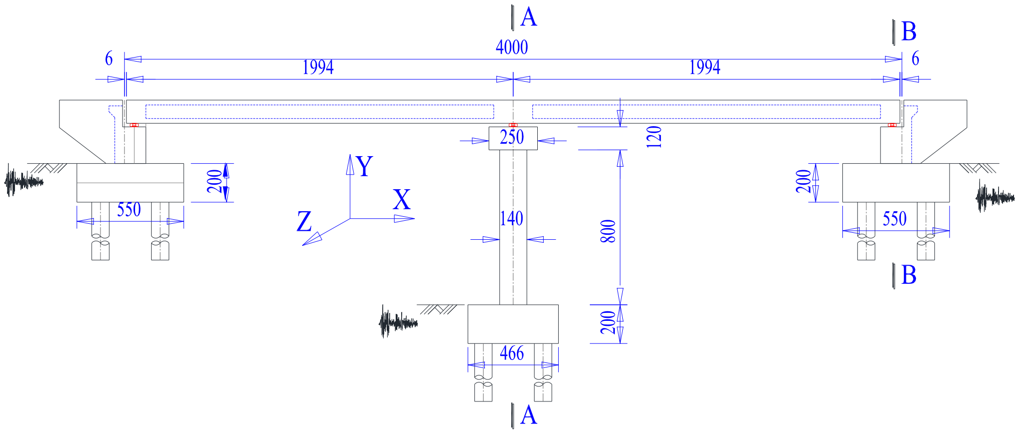

Fig. 8 Elevation of the investigated RC bridge with the SMAFSB (unit: cm)

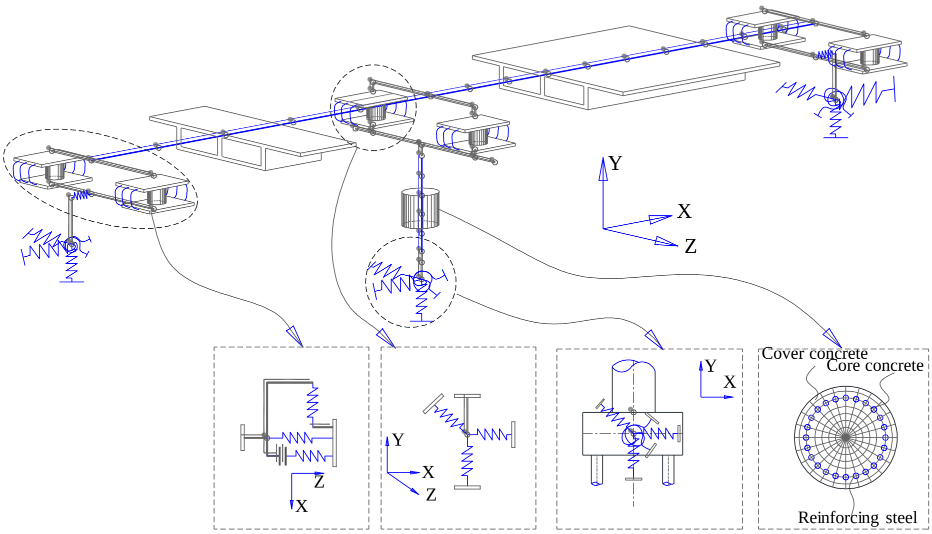

Fig. 9 FE model of the RC bridge with the SMASCFBs.

in Fig. 8. The width of the RC girder is 12.5 m. The diameter of the single RC pier is 1.4 m. The clear height of the column is 8.0 m. The widths of the bent cap and the pile cap are 8.36 m and 7.0 m, respectively. The back wall of the abutment is 2.53 m in height, 9.34 m in width and 0.40 m in thickness. The diameters of longitudinal and transversal reinforcing bars in the RC pier are 32 mm and 16 mm, respectively. The internal distance between two neighboring transverse reinforcement bars is 0.15 m. The longitudinal and transversal reinforcement ratios of the RC pier are 1.25% and 0.2%, respectively. The yield strength (F_y) of the reinforcing bar is 280.0 MPa. The concrete strength is 30.0 MPa at 28 days. The elastic moduli of the reinforcement (E_s) and the concrete (E_c) are 2.0×10^5 and 3.0×10^4 MPa, respectively. The width of the expansion joint at left and right abutments equals to 60 mm for the movement of the girder due to temperature load. To reduce the seismic damage to the bridge, the fixed SMAFSBs and movable SMAFSBs are placed on the bent cap and two abutments, respectively. The gap of the movable SMAFSB is a constant value (i.e., 60 mm) whereas the gap size of the fixed SMAFSBs should be optimized to reach a seismic damage mitigation balance between the seismically vulnerable components of the RC pier and the fixed SMAFSB.

3.1 FE model of the prototype bridge

A 3D finite element (FE) model of the RC bridge is established by using OpenSees (Mazzoni *et al*. 2007). Fig. 9 shows the schematic model together with detailed modeling information of the continuous RC bridge. The RC girder and abutment are modeled by using linear elastic beam-column elements. The movable and fixed SMAFSBs are placed on the two abutments and bent cap, respectively. They are both modeled by zero-length spring elements in parallel. The expansion joints on the left and right abutments are both modeled by zero-length element. The RC pier is modeled by the displacement-based nonlinear fiber element which considers the nonlinear characteristics of both concrete and reinforcement. The soil-structure

Table 3 Summary of DIs and corresponding LSs for RC column and bearing

Bridge component		DI	Slight (DS=1)	Moderate (DS=2)	Extensive (DS=3)	Collapse (DS=4)
Column	(a)	Physical phenomenon	Cracking and spalling	Moderate cracking and spalling	Degradation without collapse	Failure leading to collapse
	(b)	Curvature ductility (μ_k)	$\mu_k > 1$	$\mu_k > 2$	$\mu_k > 4$	$\mu_k > 7$
Bearing	(c)	Displacement (δ)	δ > 0mm	δ > 50mm	δ > 100 mm	δ > 150 mm

(a) HAZUS (2003); (b) Choi et *al*. (2004)

interaction (SSI) effect of the soil-abutment-pile-foundation is modeled by several zero-length spring elements in parallel.

3.2 FE model of the RC pier

The displacement-based Euler-Bernoulli frame element with distributed plasticity, which has four Gauss-Legendre integration points along its length, is used to investigate the nonlinear behavior of the RC columns under earthquakes. The constitutive behavior of the reinforcing bar is modeled through a uniaxial Menegotto-Pinto constitutive model with the linear kinematic hardening and aero isotropic hardening (Menegotto and Pinto 1973, Barbato and Conte 2006). The uniaxial Kent-Scott-Park concrete model presented by Scott *et al.* (1982) is employed to model the unconfined and confined concrete. A total of 2 and 6 fiber layers are divided along the radius direction for the unconfined and confined concrete, respectively. There are 24 fibers that are divided along the perimeter direction for the unconfined and confined concrete, as shown in Fig. 9.

3.3 FE model of the abutment and pile foundation

The SSI effect between the abutment, pile foundation and soil is considered in the FE model (CLATRANS 2010). Several zero-length spring elements in parallel are used to consider the SSI between the abutment, pile foundation, and soil (Maragakis *et al.* 1991). A tri-linear hysteretic model is assigned to a zero-length spring element to model the dynamic mechanism of the SSI between the soil and abutment. The tri-linear hysteretic model is composed of three regions: (i) a zero stiffness region models the expansion gap; (ii) a realistic stiffness region simulates the embankment fill response; and (iii) a yielding stage region accounts for ultimate longitudinal force capacity.

3.4 Key parameters of the FE model of the SMAFSB

The hysteretic model of the SMAFSB has been described in previous section. For the frictional sliding bearing component, the initial elastic stiffness per millimeter (k_e) and the frictional coefficient (μ) are 123.0 kN/mm and 0.03, respectively. The key parameters of the SMA-cable component used in the present SMAFSB can be calculated according to its configuration and characteristics tabulated in Table 2.

4. Seismic vulnerability analysis

Fragility curve is usually used to assess seismic vulnerability of bridges under designated earthquake intensities. The seismic demand and capacity models should be provided before calculating fragility curve. The probabilistic seismic demand model (PSDM) is a benchmark approach which can be used to derive the seismic demands based on a series of nonlinear time history seismic analyses. Cornell *et al.* (2002) proposed relation between the mean value of engineering demand parameters (*EDP*s) such as curvature ductility, bearing displacement and drift ratio to the ground motion intensity measures (*IM*s), as formulated (Nielson and Desroches 2007, Dong *et al.* 2013)

$$EDP = a \cdot (IM)^b \tag{5}$$

in which a and b = regression parameters derived from the analytical seismic responses. If the seismic demand and capacity are given, the fragility curves can be quantified (Dong and Frangopol 2015) using fitting techniques. The damage states are usually discrete and quantified by the designated thresholds of the Damage Index (*DI*) to define different Limit States (*LS*s). Once the *IM* is known, the fragility curve is expressed as

$$P[DI \geq LS_i \mid IM] = 1 - \int_0^{LS_i} \frac{1}{\sqrt{2\pi} \cdot \xi_{EDP|IM} \cdot edp} \cdot e^{-\frac{[\ln(edp) - \ln(a \cdot IM^b)]^2}{2(\xi_{EDP|IM})^2}} d(edp) \tag{6}$$

in which LS_i = the ith LS and $\xi_{EDP|IM}$ = the standard deviation of the logarithmic distribution. The damage states (*DS*) are often discrete and are quantified by the designated thresholds of the chosen *DI* to define the start of various damage stages. Slight, moderate, extensive and collapse are four levels of the *DSs* as defined in HAZUS (2003). The capacity model expressed in terms of *DI* as a function of *EDPs* is a key to quantify the *DSs* of the vulnerable components or the bridge system. The definitions of the four levels of *DSs* corresponding to the chosen *DI* that are associated with RC column and bearings are summarized in Table 3.

4.1 Spectral acceleration of ground motions

To carry out the nonlinear time-history analysis for seismic vulnerability assessment, a suite of 41 ground motion records are selected from Pacific Earthquake Engineering Research Center Ground Motion Database

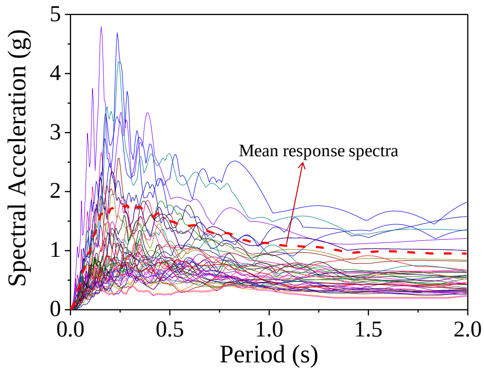

Fig. 10 Spectral acceleration of earthquake ground motions

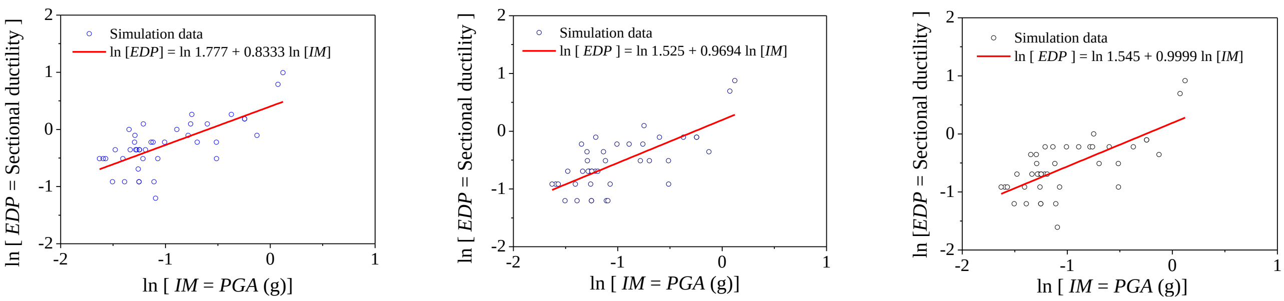

(a) 0 mm gap (b) 30 mm gap (c) 60 mm gap

Fig. 11 Relationship of logarithmic *EDP* against logarithmic *IM* of the RC pier

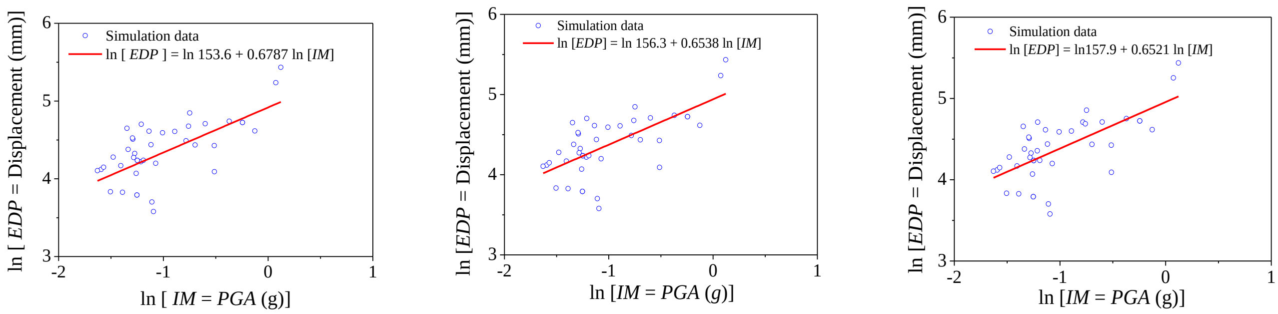

(a) 0 mm gap (b) 30 mm gap (c) 60 mm gap

Fig. 12 Relationship of logarithmic *EDP* against logarithmic *IM* of the SMAFSB

(PEER 2013). The selected ground motion records cover a range of peak ground acceleration (*PGA*) from 0.196 to 1.129g. Fig. 10 gives the acceleration response spectra with 5% damping ratio of the selected ground motion records, along with the mean amplitude of considered records. These ground motions are applied to the bridge along its longitudinal direction.

4.2 Fragility curves

Although several parameters such as *PGA*, peak ground velocity (*PGV*) and spectral acceleration can be taken as *IMs*, the previous studies (Baker and Cornell 2006, Padgett and DesRoches 2007) made a consent that the *PGA* is the most efficient, sufficient and computable parameter. PSDM is employed to establish relation between *EDPs* and *IM*. The seismically vulnerable components of the investigated bridge are the RC pier and SMAFSBs on the bent cap and two abutments, of which the fragility curves can be calculated based on Eq. (6). For the RC pier of the novel bridge with three gap sizes (i.e., 0, 30, and 60 mm), taking maximum curvature ductility at plastic hinge of the RC pier as the *EDP*, the three sets of constants *a*, *b*, and $\xi_{EDP|IM}$ can be obtained by regression analysis, as presented in Table 4. The relevant regression parameters associated with the SMAFSBs of the novel bridge with three gap sizes can also be calculated, as listed in Table 4. The relationships between the logarithmic *EDPs* (i.e., curvature ductility and bearing displacement) against *IM* of the RC pier and the SMAFSB are shown in Figs. 11 and12, respectively.

Table 4 PSDMs for different *EDPs*

SMAFSB type	Curvature ductility			Bearing displacement		
	a	b	$\xi_{EDP\|IM}$	a	b	$\xi_{EDP\|IM}$
Gap = 0 mm	1.777	0.8333	0.3305	153.6	0.6787	0.2784
Gap = 30 mm	1.525	0.9694	0.3547	156.3	0.6538	0.2336
Gap = 60 mm	1.545	0.9999	0.3739	157.9	0.6521	0.2974

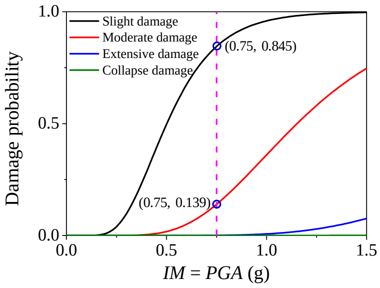

(a) 0 mm gap

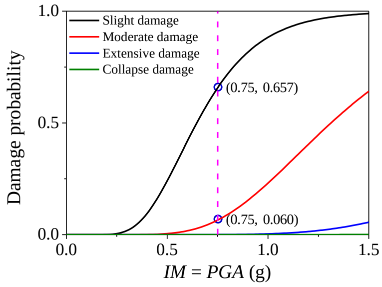

(b) 30 mm gap

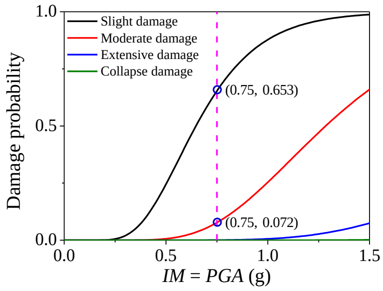

(c) 60 mm gap

Fig. 13 Fragility curves of the RC pier

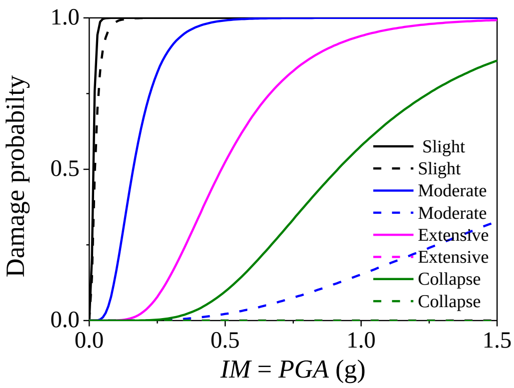

Fig. 14 Fragility curve comparison between the movable and fixed SMAFSBs

The fragility curves of the RC pier of the bridge using fixed SMAFSB with three gap sizes are plotted in Fig. 13. It can be observed from Fig. 13, that both the slight and moderate damage probabilities (i.e., 84.5% and 13.9%) associated with the gap size of 0 mm are much larger than those (i.e., 65.7% and 6.0%; 65.3% and 7.2%) associated with the gap sizes of 30 and 60 mm when the *PGA* equals to 0.75 g. The difference of the slight damage probabilities between the RC pier associated with the gap sizes of 30 mm and 60 mm is small when the *PGA* is 0.75 g. Whereas the moderate damage probability (i.e., 6.0%) of the RC pier associated with the gap size of 30 mm is a bit smaller than that (i.e., 7.2%) of the RC pier associated with the gap size of 60 mm when the *PGA* is 0.75 g. When the *PGA* is less than 1.5 g, the extensive and collapse damage probabilities of the RC pier regardless of the gap size are all less than 10.0%. It can be concluded that the SMAFSB with the gap size of 0 mm always results in larger damage probability than that with the gap size of 30 mm or 60 mm at component level (i.e., RC pier). Moreover, the seismic damage mitigation effect of the fixed SMAFSB with the gap size of 30 mm is found to perform better than the gap size of 60 mm.

A total of two types of the SMAFSB are employed in the investigated bridge: one type is the movable SMAFSBs on the two abutments and the other type is the fixed SMAFSBs on the bent cap. The fragility curves of the two types of the SMAFSB are conducted. As an example, the fragility curves of the fixed SMAFSB with the gap size of 30 mm and the movable SMAFSB with a constant gap size of 60 mm are shown in Fig. 14, respectively. It can be observed from Fig. 14 that regardless of the *DSs*, damage probabilities of the fixed SMAFSB, indicated by the solid lines, are much larger than the movable SMAFSB, indicated by the dash lines. Therefore, the fixed SMAFSBs on the pier are selected as the vulnerable components, considering the seismic mitigation assessment at both component and system levels.

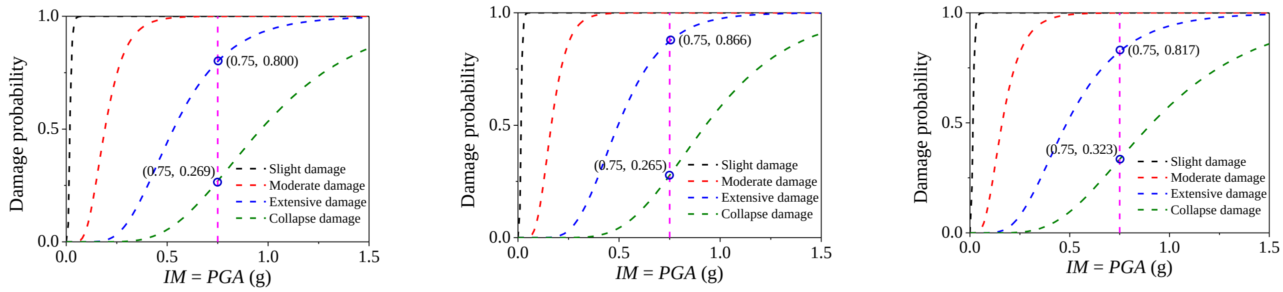

(a) 0 mm gap (b) 30 mm gap (c) 60 mm gap

Fig. 15 Fragility curves of the SMAFSB

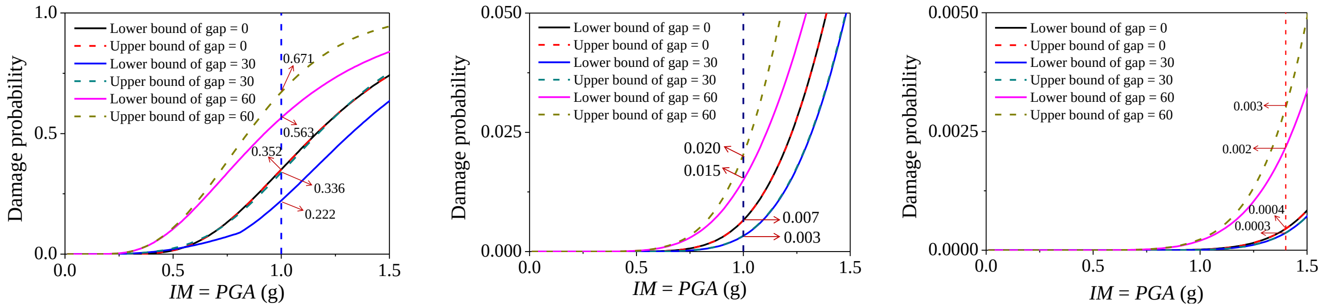

(a) moderate damage (b) extensive damage (c) collapse damage

Fig. 16 Fragility curves for bridge system with the SMAFSB

The fragility curves of fixed SMAFSBs with three gap sizes are displayed in Fig. 15. It can be concluded from Figs. 14 and 15, that the damage probabilities of the fixed SMAFSBs are much higher than the RC pier in terms of four *DSs*, indicating that fixed SMAFSB dominants the damage probability over the RC pier at bridge system level. The differences observed between the slight and moderate damage probabilities of the fixed SMAFSBs associated with three gap sizes are very small. When the *PGA* is equal to 0.75 g, the extensive damage probability of the SMAFSB with the gap of 30 mm (86.6%) is slightly higher than the SMAFSB with the gap size of 0 mm (80.0%) and 60 mm (81.7%), whereas the collapse damage probability of the SMAFSB with the gap of 30 mm (26.5%) is lower as compared to the gap sizes of 0 and 60 mm (i.e., 26.9% and 32.3%).

Given the fragility curves of vulnerable components at component level of a bridge, the fragility curve at system level can be developed for assessing structural performance, as a series, parallel, or series-parallel system. For instance, the entire bridge is assumed as a series system in this study. The fragility curves of the bridge system associated with moderate, extensive and collapse damage states are shown in Figs. 16(a)-16(c), respectively. It can be observed that the highest damage probabilities for the moderate damage probabilities of the bridge system with the gap size of 60 mm. For instance, when the *PGA* is 1.0 g, the upper and lower damage probabilities of the bridge system with the gap size of 60 mm are 67.1% and 56.3%, respectively, which is much higher than those (i.e., 35.2% and 35.3% , 33.6% and 22.2%) of the bridge system with the gap size of 0 or 30 mm. The similar trends can also be found in the extensive and collapse *DS*s. The damage probability of the bridge system with the gap size of 30 mm is the smallest among the bridge system with the three gap sizes. Consequently, the fixed SMAFSB with the gap size of 30 mm is the most effective one for mitigating the seismic damage to the bridge at system level.

5. Conclusions

A resilient SMAFSB with self-adaptive gap size is proposed to mitigate seismic damage to bridges. A 1D constitutive hysteretic model for the SMAFSB is developed for numerical simulation in seismic analysis, taking into account the effects of the friction sliding, the gap size, the self-centering and energy dissipating. A two-span continuous RC bridge is taken as the example for investigating the effectiveness of the fixed SMAFSB with self-adaptive gap size on the seismic mitigation of the bridge system.

The proposed SMAFSBs not only inherit properties of self-centering, super-elasticity, high energy dissipation from the SMA-cable component, but also possess properties of modularity, replaceability, self-adaptive damage mitigation capacity due to novel product design. The movable SMASCFB and RC pier are the two vulnerable components in the investigated resilient bridge. The fixed SMASCFB has lower damage probability as compared to movable SMASCFB. The fixed SMAFSB with appropriate gap size can effectively balance the seismic demands of the movable

SMAFSB and the RC pier at component level. The fixed SMAFSB with appropriate gap size can significantly reduce the seismic damage to the bridge at system level.

Acknowledgments

The authors are grateful for the financial support from the natural science foundation of the Shanghai Pujiang Program (Grant No. 16PJ1409600), the National Natural Science Foundation of China (Grant No. 51678463), the Chenguang Science and Technology Plan of Wuhan (Grant no. 2016070204010107), and the National Natural Science Foundation of China (Grant No. 51808476). The opinions and conclusions presented in this paper are those of the authors and do not necessarily reflect the views of the sponsoring organizations.

References

Alam, M.S., Bhuiyan, M.R. and Billah, A.M. (2012), "Seismic fragility assessment of SMA-bar restrained multi-span continuous highway bridge isolated by different laminated rubber bearings in medium to strong seismic risk zones", *Bull. Earthq. Eng.*, **10**(6), 1885-1909.

Baker, J.W. and Allin Cornell, C. (2005), "A vector-valued ground motion intensity measure consisting of spectral acceleration and epsilon", *Earthq. Eng. Struct. D.*, **34**(10), 1193-1217. https://doi.org/10.1002/eqe.474.

Barbato, M. and Conte, J.P. (2006), "Finite element structural response sensitivity and reliability analyses using smooth versus non-smooth material constitutive models", *Int. J. Reliab. Saf.*, **1**(1-2), 3-39.

Bhuiyan, A., Okui, Y., Mitamura, H. and Imai, T. (2009), "A rheology model of high damping rubber bearings for seismic analysis: Identification of nonlinear viscosity", *Int. J. Solids Struct.*, **46**(7-8), 1778-1792. https://doi.org/10.1016/j.ijsolstr.2009.01.005.

Brinson, L.C. (1993), "One-dimensional constitutive behavior of shape memory alloys: thermomechanical derivation with non-constant material functions and redefined martensite internal variable", *J. Intel. Mat. Syst. Str.*, **4**(2), 229-242. https://doi.org/10.1177/1045389X9300400213

Caltrans, S. (2010), *Seismic Design Criteria, Ver. 1.6*, California Dept. of Transportation, Sacramento, California,USA.

Choi, E. (2002), "Seismic analysis and retrofit of mid-America bridges", School of Civil and Environmental Engineering, Georgia Institute of Technology.

Choi, E., DesRoches, R. and Nielson, B. (2004), "Seismic fragility of typical bridges in moderate seismic zones", *Eng. Struct.*, **26**(2), 187-199. https://doi.org/10.1016/j.engstruct.2003.09.006.

Choi, E., Nam, T.h. and Cho, B.S. (2005), "A new concept of isolation bearings for highway steel bridges using shape memory alloys", *Can. J. Civil Eng.*, **32**(5), 957-967. https://doi.org/10.1139/l05-049.

Cornell, C.A., Jalayer, F., Hamburger, R.O. and Foutch, D.A. (2002), "Probabilistic basis for 2000 SAC federal emergency management agency steel moment frame guidelines", *J. Struct. Eng.*, **128**(4), 526-533. https://doi.org/10.1061/(ASCE)0733-9445(2002)128:4(526).

DesRoches, R., Pfeifer, T., Leon, R.T. and Lam, T. (2003), "Full-scale tests of seismic cable restrainer retrofits for simply supported bridges", *J. Bridge Eng.*, **8**(4), 191-198. https://doi.org/10.1061/(ASCE)1084-0702(2003)8:4(191).

Dezfuli, F.H. and Alam, M.S. (2014), "Performance-based assessment and design of FRP-based high damping rubber bearing incorporated with shape memory alloy wires", *Eng. Struct.*, **61**, 166-183. https://doi.org/10.1016/j.engstruct.2014.01.008.

Dezfuli, F.H. and Alam, M.S. (2016), "Seismic vulnerability assessment of a steel-girder highway bridge equipped with different SMA wire-based smart elastomeric isolators", *Smart Mater. Struct.*, **25**(7), 075039.

Dion, C., Bouaanani, N., Tremblay, R. and Lamarche, C.P. (2011a), "Real-time dynamic substructuring testing of a bridge equipped with friction-based seismic isolators", *J. Bridge Eng.*, **17**(1), 4-14. https://doi.org/10.1061/(ASCE)BE.1943-5592.0000199.

Dion, C., Bouaanani, N., Tremblay, R., Lamarche, C.P. and Leclerc, M. (2011b), "Real-time dynamic substructuring testing of viscous seismic protective devices for bridge structures", *Eng. Struct.*, **33**(12), 3351-3363. https://doi.org/10.1016/j.engstruct.2011.06.021.

Dolce, M., Cardone, D. and Marnetto, R. (2000), "Implementation and testing of passive control devices based on shape memory alloys", *Earthq. Eng. Struct. D.*, **29**(7), 945-968.

Dolce, M., Cardone, D. and Palermo, G. (2007), "Seismic isolation of bridges using isolation systems based on flat sliding bearings", *Bull. Earthq. Eng.*, **5**(4), 491-509.

Dong, Y. and Frangopol, D.M. (2016), "Performance-based seismic assessment of conventional and base-isolated steel buildings including environmental impact and resilience", *Earthq. Eng. Struct. D.*, **45**(5), 739-756. https://doi.org/10.1002/eqe.2682.

Dong, Y. and Frangopol, D.M. (2016), "Probabilistic time-dependent multihazard life-cycle assessment and resilience of bridges considering climate change", *J. Perform. Constr. Fac.*, **30**(5), 04016034. https://doi.org/10.1061/(ASCE)CF.1943-5509.0000883.

Dong, Y. and Frangopol, D.M. (2015), "Risk and resilience assessment of bridges under mainshock and aftershocks incorporating uncertainties", *Eng. Struct.*, **83**, 198-208. https://doi.org/10.1016/j.engstruct.2014.10.050.

Dong, Y., Frangopol, D.M. and Saydam, D. (2013), "Time-variant sustainability assessment of seismically vulnerable bridges subjected to multiple hazards", *Earthq. Eng. Struct. D.*, **42**(10), 1451-1467. https://doi.org/10.1002/eqe.2281.

Fang, C., Wang, W., He, C. and Chen, Y. (2017), "Self-centring behaviour of steel and steel-concrete composite connections equipped with NiTi SMA bolts", *Eng. Struct.*, **150**, 390-408. https://doi.org/10.1016/j.engstruct.2017.07.067.

Fang, C., Yam, M. C., Lam, A.C. and Xie, L. (2014), "Cyclic performance of extended end-plate connections equipped with shape memory alloy bolts", *J. Constr. Steel Res.*, **94**, 122-136. https://doi.org/10.1016/j.jcsr.2013.11.008.

Fang, C., Zheng, Y., Chen, J., Yam, M.C.H. and Wang, W. (2019), "Superelastic NiTi SMA cables: thermal-mechanical behavior, hysteretic modelling and seismic application", *Eng. Struct.*, **183**, 533-549. https://doi.org/10.1016/j.engstruct.2019.01.049.

FEMA, H. (2003), "Multi-hazard loss estimation methodology, earthquake model", *Washington, DC, USA: Federal Emergency Management Agency*.

Ghobarah, A. and Ali, H. (1990), "Seismic design of base-isolated highway bridges utilizing lead–rubber bearings", *Can. J. Civil Eng.*, **17**(3), 413-422. https://doi.org/10.1139/l90-045.

Hall, J.F., Holmes, W.T. and Somers, P. (1996), *Northridge earthquake of January 17, 1994: reconnaissance report*, Earthquake Engineering Research Institute.

Johnson, R., Padgett, J.E., Maragakis, M.E., DesRoches, R. and Saiidi, M.S. (2008), "Large scale testing of nitinol shape memory alloy devices for retrofitting of bridges", *Smart Mater. Struct.*, **17**(3), 035018.

Liang, C. and Rogers, C. (1992), "Design of shape memory alloy actuators", *J. Mech. Des.*, **114**(2), 223-230.

Liu, J.l., Zhu, S., Xu, Y.L and Zhang, Y. (2011), "Displacement-based design approach for highway bridges with SMA isolators", *Smart Struct. Syst.*, **8**(2), 173-190. http://dx.doi.org/10.12989/sss.2011.8.2.173.

Maragakis, E., Douglas, B. and Vrontinos, S. (1991), "Classical formulation of the impact between bridge deck and abutments during strong earthquakes", *Proceedings of the 6th Canadian Conference on Earthquake Engineering*, 205-212.

Mazzoni, S., McKenna, F., Scott, M., Fenves, G. and Jeremic, B. (2007), "*OpenSees Command Language Manual*", Pacific Earthquake Engineering Research Center, University of California, Berkley, CA, USA.

Menegotto, M. and Pinto, P.E. (1973), "Method for analysis of cyclically loaded reinforced concrete plane frames including changes in geometry and non-elastic behavior of elements under combined normal force and bending", *Proceedings of the IABSE Symposium on Resistance and Ultimate Deformability of Structures Acted on by Well-Defined Repeated Loads*, Lisbon, Portugal.

Qiu, C. and Zhu. S. (2017), "Performance-based seismic design of self-centering steel frames with SMA-based braces", *Eng. Struct.*, **130**, 67-82. https://doi.org/10.1016/j.engstruct.2016.09.051.

Qiu, C. and Zhu. S. (2017), "Shake table test and numerical study of self-centering steel frame with SMA braces", *Earthq. Eng. Struct. D.*, **46**,117-137. https://doi.org/10.1002/eqe.2777.

Qiu, C., Li, H., Ji, K., Hou, H. and Tian, L. (2017), "Performance-based plastic design approach for multi-story self-centering concentrically braced frames using SMA braces", *Eng. Struct.*, **153**, 628-638. https://doi.org/10.1016/j.engstruct.2017.10.068.

Qiu, C., Zhang, Y., Li, H., Qu, B., Hou, H. and Tian, L. (2018), "Seismic performance of Concentrically Braced Frames with non-buckling braces: A comparative study", *Eng. Struct.*, **154**, 93-102. https://doi.org/10.1016/j.engstruct.2017.10.075.